



# Extensions of the SIESTA DFT code for simulation of molecules.

Olivier Coulaud, Patrice Bordat, Pierre Fayon, Vincent LeBris,  
Isabelle Baraille, Ross Brown

**RESEARCH  
REPORT**

**N° 8221**

February 2013

Project-Team HiePACS





## Extensions of the SIESTA DFT code for simulation of molecules.

Olivier Coulaud\*, Patrice Bordat†, Pierre Fayon †, Vincent LeBris†, Isabelle Baraille†, Ross Brown†

Project-Team HiePACS

Research Report n° 8221 — February 2013 — 27 pages

**Abstract:** We describe extensions to the SIESTA density functional theory (DFT) code [30], for the simulation of *isolated* molecules and their absorption spectra. The extensions allow for:

- Use of a multigrid solver for the Poisson equation on a finite DFT mesh. Non-periodic, Dirichlet boundary conditions are computed by expansion of the electric multipoles over spherical harmonics.
- Truncation of a molecular system by the method of design atom pseudo-potentials of Xiao and Zhang[32].
- Electrostatic potential fitting to determine effective atomic charges.
- Derivation of electronic absorption transition energies and oscillator strengths from the raw spectra produced by a recently described, order  $O(N^3)$ , time-dependent DFT code[21]. The code is furthermore integrated within SIESTA as a post-processing option.

**Key-words:** multigrid solver, DFT /TDDFT computation, molecular systems, SIESTA

---

This work was supported by A.N.R. grant "Nossi", CIS-007-005.

\* Centre de Recherche Inria Bordeaux Sud-Ouest, Olivier.Coulaud@inria.fr

† Institut pluridisciplinaire de recherches sur l'environnement et les matériaux, UMR 5624 du CNRS et de l'Université de Pau et des pays de l'Adour. Hélio parc, 2, av. du Pt. P. Angot, 64053 PAU Cedex 9, France.

**RESEARCH CENTRE  
BORDEAUX – SUD-OUEST**

200 avenue de la Vieille Tour  
33405 Talence Cedex

## Extensions du code DFT SIESTA pour la simulation de molécules.

**Résumé :** Nous décrivons les extensions au code siesta [30] de la théorie de la fonctionnelle de densité (DFT), pour la simulation des molécules isolées et leurs spectres d'absorption. Ces extensions permettent :

- l'utilisation d'un solveur multigrille pour l'équation de Poisson sur le maillage DFT. Les conditions aux limites de Dirichlet sont calculées par un développement en harmoniques sphériques du potentiel électrique ;
- la coupure du système moléculaire à l'aide du pseudo-potentiels de l'atome sur mesure de Xiao Zhang[32] ;
- le calcul des charges effectives atomiques par la méthode de l'ajustement du potentiel électrostatique ;
- Calcul des énergies de transition d'absorption électroniques et des forces d'oscillateur à partir des spectres bruts obtenus par un code DFT dépendant du temps[21]. Le code est en outre intégré dans SIESTA comme une option de post-traitement. code[21].

**Mots-clés :** solveur multigrille, calculs DFT /TDDFT système moléculaire, SIESTA

## 1 Introduction

The SIESTA program is well established in the field of simulation of solids with density functional theory (DFT)[30]. It is used in an ever widening range of applications, benefitting from regular maintenance and extensions of the code's capabilities[6, 28]. SIESTA employs numerical atomic orbitals (AO's) with strictly finite range, leading to order- $N$  scaling of computations with respect to the number of atoms. SIESTA was thus an attractive DFT engine for a new, fast time-dependent DFT (TDDFT) algorithm for molecular systems, based on use of dominant products of finite orbitals, and scaling as  $O(N^3)$  with the number of atoms  $N$ [21]. Previously, this TDDFT code used orbital and density matrix data from files produced by SIESTA. Moreover, it provided only a raw spectrum. We have therefore undertaken to couple the program directly to SIESTA and to extract transition energies and oscillator strengths from the raw spectrum. Furthermore, SIESTA remains a periodic DFT code, meaning that to simulate a molecular system, very large, essentially empty DFT meshes may be necessary to effectively isolate the system from its periodic images.

The present contribution therefore describes extensions of SIESTA useful in the field of molecular systems:

1. Adaption to molecular computations by *(i)* Computation of Dirichlet boundary conditions in the Poisson equation, by development of electric multipolar moments, up to order 4 in spherical harmonics; and *(ii)* Introduction of a multi-grid solver for the Poisson equation;
2. Introduction of an electrostatic potential fit algorithm for the assignment of atomic partial charges;
3. Implementation of 'design atom' pseudo-potentials[32], allowing truncation of a molecular system by replacing a bond by a tailor-made lone pair;
4. Direct coupling to SIESTA of the order  $O(N^3)$  TDDFT code FAST, with extraction of transition energies and oscillator strengths.

Extensions 1–3, discussed in the correspondingly numbered subsections of part 2, are available as a set of patches of SIESTA, development version 431, downloadable at

[https://gforge.inria.fr/frs/?group\\_id=1179](https://gforge.inria.fr/frs/?group_id=1179)<sup>1</sup>. The FAST DFT code is available at the same URL.

## 2 Extensions of SIESTA

### 2.1 Solution of the Poisson equation for non-periodic systems

During self-consistency cycles in a DFT computation, recourse is made at each cycle to the Hartree energy,

$$E_H = \int \rho(\mathbf{r})V(\mathbf{r})d\mathbf{r}, \quad (1)$$

approximated as a discrete sum over a mesh of points encompassing the system. The electrostatic potential,  $V(\mathbf{r})$ , itself is formally a space integral of contributions of the electronic density,  $\rho(\mathbf{r})$ ,

$$V(\mathbf{r}) = \int \rho(\mathbf{s}) \frac{1}{\|\mathbf{r} - \mathbf{s}\|} d\mathbf{s}. \quad (2)$$

---

<sup>1</sup>Access to be opened on acceptance of the present paper

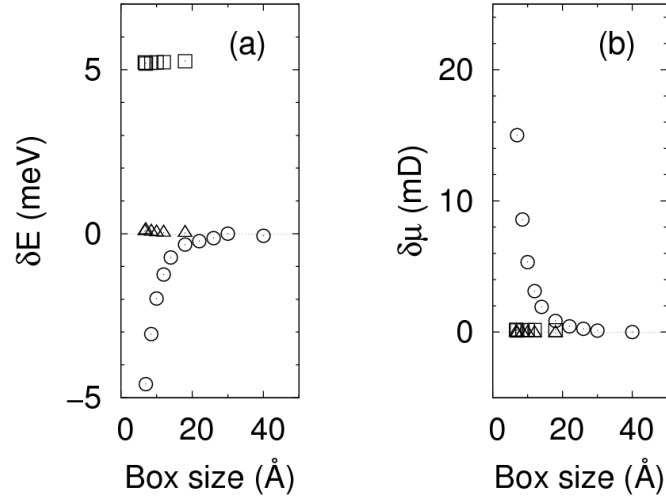


Figure 1: Convergence of the physical properties of the water molecule with respect to the side of the simulation box: (a) Energy; (b) Electric dipole moment. Symbols : ○, periodic simulation, using the standard FFT solver; □ and △, non-periodic simulation, using a second order, 7-point or a fourth order, compact 16-point stencil respectively for the Laplacian in the multi-grid solver for the Poisson equation. Data are plotted as differences with respect to the converged values (FFT, large box). See section 2.1 for simulation conditions.

Rather than directly integrating the contributions of infinitesimal volume elements of the density, it is much more efficient to solve the Poisson equation for  $V(\mathbf{r})$ :

$$\Delta V(\mathbf{r}) = -4\pi\rho(\mathbf{r})/\epsilon_0, \quad (3)$$

with suitable boundary conditions, where  $\Delta$  is the Laplacian. We refer the reader to [30] for details of implementation in SIESTA, in particular partition of the problem into neutral atom and bond contributions to  $\rho$ .

Because SIESTA is a periodic code, in which the system and the DFT mesh (typically one crystal unit cell) are replicated indefinitely in all directions, a particularly effective solution of eqn. (3) is obtained by transforming to  $\mathbf{k}$ -space using fast Fourier transforms (FFT). This method is ideal for crystals, but for finite molecular systems the DFT mesh (periodic cell) must be made large enough to damp out interactions of the system with its periodic images. Physical properties may converge only slowly with the mesh size. Figure (1a,b) illustrates this for a toy model of an isolated water molecule. Although the molecule and its orbitals hold within a cube of side 5.7 Å, a DFT mesh of side 20 Å is required to achieve good convergence of the energy ( $\approx -465.8$  eV) and dipole moment ( $\approx 1.389$  D) in the periodic FFT computation.

We refer repeatedly to this model, using the standard double-zeta with polarisation basis set of SIESTA (DZP, energy shift parameter 0.02 Ry), in the local density approximation (LDA, Ceperley-Alder exchange-correlation[25]). The mesh cutoff is 400 Ry. Heuristics in SIESTA cause the corresponding mesh step to vary slightly with the box size, in the range  $0.08 \pm 0.002$  Å in all calculations. The tolerances for convergence of the density matrix and energy are  $10^{-6}$  and  $10^{-6}$  eV respectively. Standard Troullier-Martins pseudo-potentials from the SIESTA library are used throughout. The model is used at the optimised geometry.

In fact, the solution of eqn. (3) for finite systems is determined uniquely by the values on a closed surface enclosing the charge density, *i.e.* Dirichlet boundary conditions. The DFT mesh for a finite system can thus be made quite small, provided there is a recipe for accurately specifying the solution on the surface of the DFT mesh.

A molecular computation thus needs; (i) an independent means of specifying the Dirichlet boundary conditions at the surface points of the finite DFT mesh; (ii) an efficient solver for the boundary value problem of  $V(\mathbf{r})$  in the interior of the domain.

### Dirichlet boundary conditions by expansion of multipoles over spherical harmonics.

Dirichlet boundary conditions may be determined by either of two alternative multipole expansions of  $\frac{1}{\|\mathbf{r}-\mathbf{s}\|}$  in eqn (2): Cartesian multipoles or spherical harmonics. Cartesian expansion in the inverse distance[19] is easy and cheap to compute up to second order,  $p = 2$ , but tedious to pursue to higher orders. Furthermore, the number of terms grows as  $p^3$ . Spherical harmonics cost more to evaluate, but are readily extended to any order. The number of terms grows only as  $(p+1)^2$  and their complexity is lower than in the Cartesian approach. We have implemented expansion over spherical harmonics in SIESTA. The electrostatic potential on the surface of the simulation box is approximated by an expansion up to order  $p$  as follows[18]:

$$V(\mathbf{r}) \approx V_p(\mathbf{r}) = \sum_{l=0}^p \sum_{m=-l}^l \frac{(-1)^m}{r^{l+1}} M_l^m Y_l^{-m}(\theta, \phi),$$

$$M_l^m = \int_{\mathbb{R}^3} d^3\mathbf{s} \rho(\mathbf{s}) s^l Y_l^{-m}(\mathbf{s}),$$

where  $(r, \theta, \phi)$  are the spherical coordinates of point  $\mathbf{r}$ . In practice, the electronic density  $\rho$  is known on the DFT mesh points, and non-vanishing only within the supports of the finite numerical orbitals employed in SIESTA. We allow only orthorhombic meshes for the multi-grid solver, since an arbitrary mesh is pointless for computation of an isolated molecule. Therefore, although we develop the potential over spherical harmonics on the boundaries we express them in Cartesian form. Setting  $\phi(\mathbf{s}) = s^l Y_l^{-m}(\mathbf{s})$  at mesh point  $\mathbf{s}$ , we approximate  $M_l^m$  by

$$M_l^m \approx \sum_{\mathbf{s}|\rho(\mathbf{s}) \neq 0} \rho(\mathbf{s}) \phi(\mathbf{s}) dV,$$

where  $\phi(\mathbf{s})$  is computed only at mesh-points with non-vanishing density, *i.e.* above a user-defined threshold. The volume element of the mesh is  $dV$ .

The multipole expansion converges formally for all  $\mathbf{r}$  outside the support of  $\rho(\mathbf{s})$ . Accurate Dirichlet conditions may be obtained either by: increasing the size of the DFT mesh box, improving in eqn. (2) the separation between surface points  $\mathbf{r}$  and charges at interior points  $\mathbf{s}$ ; or by increasing the order of the expansion. In DFT computations, intensive use of the mesh points drives the balance towards higher order expansion on a smaller mesh.

If the supports of the numerical orbitals impinge on the surface of the DFT mesh, accuracy is certainly compromised. In our implementation, we use the atomic coordinates, and the radii of the atomic orbitals to check for this problem. However, it is always advisable to perform a series of exploratory calculations with different box sizes and multipole orders, to prove convergence of computed properties with respect to errors in the expansion.

As can be seen from figure 1, both the total energy and the dipole moment of water are highly converged when boundary conditions are computed with fourth order spherical harmonics in a box of only 7 Å, or a clearance of barely 0.65 Å around the atomic orbitals used to develop  $\rho(\mathbf{r})$ .

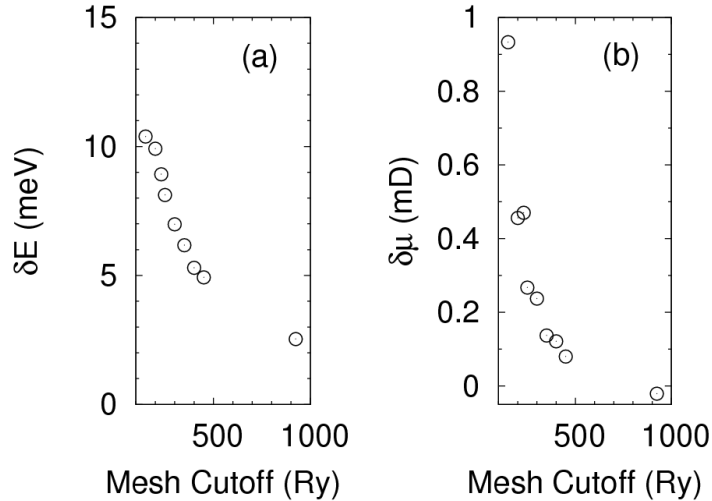


Figure 2: Dependence of the properties of the water molecule on the mesh step in the finite model with the second order MG solver, box side  $7 \text{ \AA}$ . Data are shown as differences with respect to the well converged FFT solution of a large periodic model (box side  $40 \text{ \AA}$ ). (a) Energy(ref. -465.800453 eV); (b) Dipole moment (ref. 1.3887D).

**Multi-grid solver for the Poisson equation.** Solution of the Poisson equation on a regular finite mesh proceeds by discretizing the Laplacian operator by finite differences. One obtains a system of linear equations,  $\mathbf{A}_h \mathbf{V} = \mathbf{f}$ , for  $V$  at points in the interior of the domain. Vector  $\mathbf{f}$  contains the Dirichlet conditions. The sparse, symmetric, positive definite matrix  $\mathbf{A}_h$  has the classical stripe pattern described by a 'stencil'. A 7-point second order stencil and a compact, 16-point fourth order solver have been included in the present implementation. The matrix size is  $N = N_1 \times N_2 \times N_3$  where  $N_i = L_i/h_i$  is the number of mesh points in the  $i$ -direction and  $h_i$  is the mesh step in  $i$ -direction.

Iterative methods are attractive for solving the Poisson equation inside the SCF loop, rather than direct methods like Cholesky factorization. It is well known that multi-grid solvers are the fastest iterative methods for solution of the Poisson equation in a rectangular box. The complexity is linear in the system size, even better than for a periodic solver based on FFT. Reference[8] discusses multigrid methods (MG) in detail. One efficient parallel multigrid software package is the HYPRE software library [13, 4, 2]. Here, we wrap this general library to make it available within SIESTA. We use the structured-grid interface and either PFMG, a semicoarsening multi-grid solver that uses pointwise relaxation, or preconditioned conjugate gradients (PCG)[12]. The PFMG solver allows different parallel smoothers, including the red-black Gauss-Seidel method. The PGC method uses PFMG as a preconditioner. Our wrapper is very flexible and can be extended easily to more complex operators like higher order discretizations of the Laplacian. Different kinds of mesh distribution are also available. We use classical, uniform 2-D real-space domain decomposition and the new SIESTA parallelization scheme based on balanced real-space domain decomposition, achieved with a recursive bisection algorithm[28]. Ideally, an irregular or even unstructured mesh would adjust to the gradient of the electronic density, leading to a finite element formulation of the problem, a future refinement possible within the HYPRE library.



**Performance.** Implementation of the HYPRE MG solver was checked by generating the Dirichlet conditions for distributions of point charges, numerically solving the Poisson equation in empty space and checking the solution against the known analytical result. The embedding of the MG solver in SIESTA was checked by comparing to results with the standard FFT in SIESTA, on the toy model of water mentioned above. In what follows we found it sufficient to expand the Dirichlet boundary conditions over spherical harmonics up to order four.

Figure (1a,b) shows, for the same mesh step in the FFT and MG calculations (0.08 Å or plane wave cutoff of 400 Ry), the superior convergence of the physical properties with the finite box size, achievable with the MG solver and Dirichlet conditions, compared to that of the solution under periodic boundary conditions, with the FFT solver. For the given mesh step, the energy obtained with the second order MG solver is 5 meV higher than the FFT solution, and the dipole moment 0.1 mD larger. Indeed, the final accuracy of the DFT computation depends on the step of the DFT mesh and on the order of discretization of the operator. The energy obtained with the second order discrete Laplacian operator is converged with respect to box size, but to a value significantly different from the FFT result. The fourth order approximation, using a 16-point stencil, on the other hand, gives the same results as the FFT calculation. Figure (2a,b) confirms convergence of the MG solutions to the FFT values as the step size is reduced, for the second order solver, where the effect is most significant. Figure 1 of the supplementary information(SI) shows the linear scaling of the algorithm with the system size.

## 2.2 Electrostatic potential fit of partial atomic charges

Often it is desirable to assign charges to atomic centres, to be used as proxies for the full electronic density  $\rho(\mathbf{r})$ . Such schemes, *e.g.* Mulliken charges and 'atoms in molecules' analysis[31], each have their own advantages and disadvantages. In classical molecular dynamics, partial atomic charges 'best fit' to represent the Coulomb forces would be desirable. In practice, 'best fit' representation of the Coulomb potential itself is much more tractable analytically and more common than fitting the gradient of the potential.

We therefore have added such an electrostatic potential (ESP) fit routine to SIESTA. This is a classic problem[7, 16, 29]. Here we give the minimum details to describe our implementation. The problem is to determine a set of partial atomic charges  $q_i, i = 1, \dots, N$  on  $N$  atomic centres  $\mathbf{R}_i$ , such that their Coulomb potential is a good approximation to the full molecular potential at a set of test points  $\mathbf{S}_j, j = 1, \dots, M$ , commonly chosen near the molecular van der Waals surface. Let  $U_j$  be the full molecular electrostatic potential at  $\mathbf{S}_j$ :

$$U_j = - \int_{\mathbb{R}^3} d^3\mathbf{r} \frac{\rho(\mathbf{r})}{|\mathbf{r} - \mathbf{S}_j|} + \sum_{i=1}^N \frac{Z_i}{|\mathbf{R}_i - \mathbf{S}_j|},$$

where  $Z_i$  is the nuclear charge on atom  $i$  (in the case of pseudo-potentials, the valence charge). These values are to be approximated by

$$V_j = \sum_{i=1}^N \frac{q_i}{|\mathbf{R}_i - \mathbf{S}_j|},$$

where the partial charges  $q_i$  are determined by least squares minimisation of the error

$$\chi^2(\{q_i\}) = \sum_{j=1}^M (U_j - V_j)^2.$$

As usual, we add *via* a Lagrangian multiplier,  $\lambda$ , the constraint that the  $q_i$  should sum to the total charge of the molecule,  $Q$ . The problem is then to find stationary points (minima) of the Lagrangian

$$L(\{q_i\}, \lambda) = \chi^2(\{q_i\}) + \lambda \left( \sum_{i=1}^N q_i - Q \right).$$

After a little algebra one finds the  $q_i$  (and multiplier  $\lambda$ ) as solutions of an  $(N + 1) \times (N + 1)$  linear system, the matrix equation

$$\mathbf{A}' \mathbf{q}' = \mathbf{b}', \quad (4)$$

with

$$\mathbf{A}' = \begin{pmatrix} & & & 1 \\ & \Sigma \Sigma^T & & \vdots \\ & & & 1 \\ 1 & \dots & 1 & 0 \end{pmatrix}, \quad \mathbf{q}' = \begin{pmatrix} \vdots \\ q_i \\ \vdots \\ \lambda \end{pmatrix}, \quad \mathbf{b}' = \begin{pmatrix} \vdots \\ \sum_{j=1}^M U_j / s_{ij} \\ \vdots \\ Q \end{pmatrix}.$$

$\Sigma$  is the  $N \times M$  matrix with elements  $\Sigma_{ij} = 1/s_{ij}$ , with  $s_{ij} = |\mathbf{R}_i - \mathbf{S}_j|$ .

It long has been known[16] that matrix  $\mathbf{A}'$  may be ill-conditioned or singular, depending on the choice of the test points  $\mathbf{S}_j$ , because the far field of a set of charges is determined principally by their lowest order multipoles. In our implementation we use as  $\mathbf{S}_j$ 's a subset of the DFT mesh points, since the full electrostatic potential is known already on the DFT mesh at the end of the SCF cycles. Similar to a Connolly surface[11], the mesh points chosen are those at least at a distance  $R_{\min}$  from all nuclei, and at most  $R_{\min} + \delta R$  from some nucleus (the 'skin' thickness  $\delta R$  being in practice  $\approx 0.1 \text{ \AA}$ ). Our experience with the finite support AO's in SIESTA is that ESP charges are physically sensible and relatively insensitive to  $R_{\min}$  when it is chosen from just greater than the largest AO radius, up to around  $5 \text{ \AA}$  beyond. For larger values, matrix  $\mathbf{A}'$  may indeed become singular. Typical mesh sizes generally lead to several thousand points within the skin, so that the main cause of any indetermination of the charges is the singularity of  $\mathbf{A}'$  when all the points are chosen too far away from the molecule.

We solve equation (4) using a truncated SVD algorithm, starting with  $QR$  factorization of  $\mathbf{A}'$  as  $\mathbf{A}' = \mathbf{Q}\mathbf{R}$ , where  $\mathbf{Q}$  is an orthogonal matrix and  $\mathbf{R}$  is upper triangular. Singular value decomposition of  $\mathbf{R}$  yields  $\mathbf{R} = \mathbf{U}\mathbf{W}\mathbf{V}^T$ , where  $\mathbf{U}$  and  $\mathbf{V}$  are orthogonal and  $\mathbf{W}$  is diagonal (diagonal elements  $w_i$ ). Small singular eigenvalues, signifying singularity of the matrix and indetermination of the  $q_i$ , are removed by setting  $w_i = 0$  if  $|w_i/w_{\max}| < \epsilon$ . We standardly choose  $\epsilon = 10^{-9}$ . The solution,  $\mathbf{q}'$ , of eqn. (4) is then

$$\mathbf{q}' = \mathbf{V}\mathbf{W}^{-1}\mathbf{U}^T\mathbf{Q}^T\mathbf{b}'.$$

Routines from the BLAS[23] and LAPACK[5] libraries are used here to perform these operations. The calculation is parallel.

Figure (3) shows the ESP charges found for polar groups in indigo, as a function of the ESP shell radius  $R_{\min}$  ( $\delta R = 0.1 \text{ \AA}$ ). Conditions are the same as for the toy water model in section 2.1. The Poisson equation was solved with the multi-grid method with Dirichlet boundary conditions from spherical harmonics up to order 4. It will be observed that the ESP charges are insensitive to  $R_{\min}$  once the sample points are all outside the largest atomic orbital (radius  $\sim 2.6 \text{ \AA}$ ). The charges on C,O,N and H are 0.28, -0.34, -0.42 and 0.29e.

### 2.3 Truncation of molecules with design atom pseudo-potentials

It often is desirable to restrict the size of a quantum mechanical calculation to just the essential atoms for the problem at hand. Quantum mechanics/molecular mechanics (QM/MM) calculations

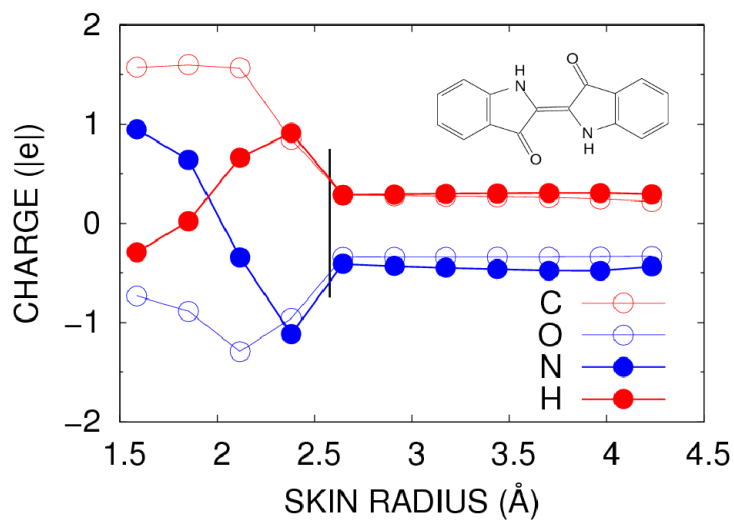


Figure 3: ESP charges on the polar groups C=O and NH in indigo (inset), as a function of the radius of the 'skin' of DFT mesh points used in the ESP fit. The vertical line shows the largest atomic orbital radius.

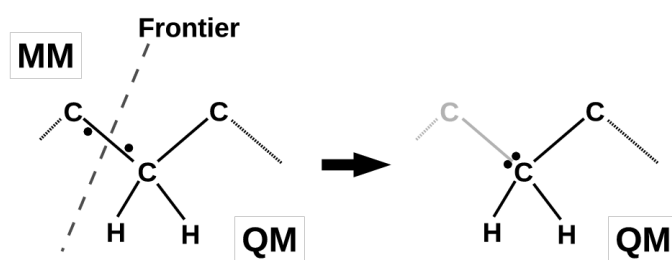


Figure 4: Truncation of a large molecule in a QM/MM model by cutting a bond and completing the dangling valence with an electron to form a lone pair mimicking the missing bond.

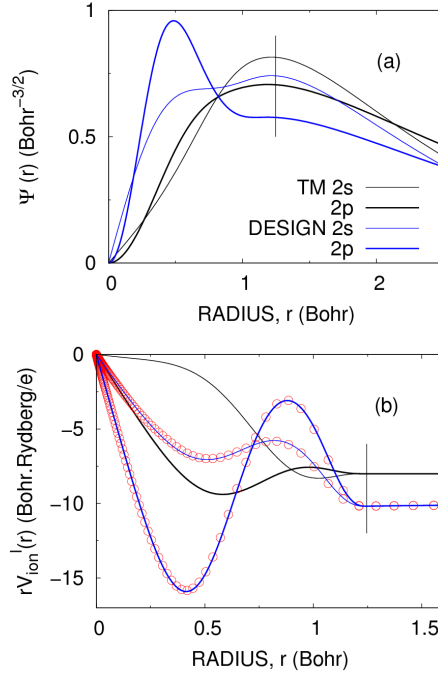


Figure 5: Comparison of design atom and standard Troullier-Martins pseudo-potentials for the 2s (thin) and 2p (thick lines) shells of carbon. Black: standard Troullier-Martins method, blue: design atom method, this work. Vertical lines: core radius. (a) Wave functions, showing squeezing from outside to inside the core to maintain the valence density of standard carbon; (b) Ionic pseudo-potentials, showing deepening in the core to accommodate the extra electronic density. Points: reference data kindly provided by Y. Zhang.

are a prime example, as are cluster calculations in which a cluster of atoms of tractable size is cut out of a periodic material. In both cases it is necessary to correct dangling valencies left by the truncation, to reduce perturbation of the core region of the cluster. One way is to add capping atoms (usually hydrogens) to complete peripheral valencies.

Another is to turn dangling bonds into lone pairs, an approach developed by Xiao and Zhang[32] with a view to QM/MM calculations, *cf.* figure (4). Perturbation of the core of the cluster is then minimised by transforming the peripheral atom so capped into a 'design' atom, with specific pseudo-potentials to mimic the electronic structure of the atom it replaces. We have extended this method to truncation on oxygen and applied it to larger systems, where we find the perturbation decays rapidly with distance from the cut bond.

Pseudo-potentials may be produced and tested with the help of the ATOM program distributed with SIESTA. We coded 'design' Troullier-Martins, norm conserving pseudo-potentials in ATOM. In the design atom approach for carbon, one adds an electron and increases the nuclear charge by one unit. But the design atom is not just nitrogen, since to minimise discrepancies between the full and the truncated molecule, it is further required that the electronic density of the design atom outside the core matches that of carbon. This constraint is achieved by rescaling the wave functions outside the core radius, per angular momentum channel,  $l$ , by  $\eta_l = (N_l/N_l^D)^{1/2}$ , where  $N_l$  is the number of valence electrons of the original atom in shell  $l$  and  $N_l^D$  that in the same shell of the design atom.

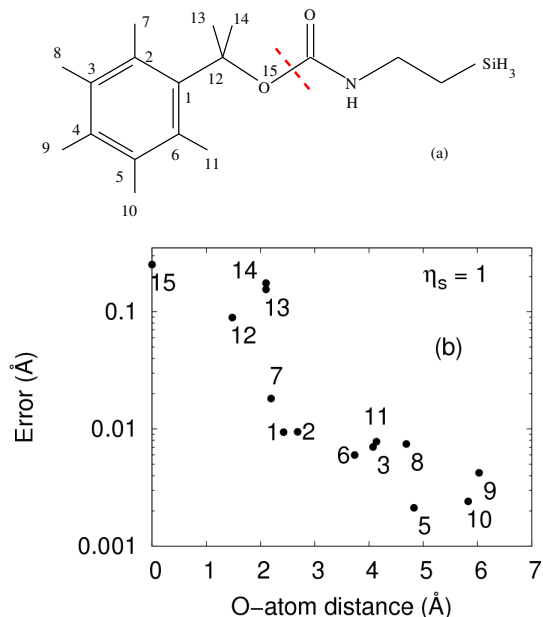


Figure 6: Use of a design atom oxygen to truncate a benzyl carbamate model of a graftable dye: (a) Structure, indicating the bond cut and replaced by a lone pair; (b) Errors in the positions of atoms in the truncated molecule with respect to the full molecule (numbering as in (a)).

Thus, for carbon,  $\eta_{2p} = \sqrt{2/3}$ , and one expects  $\eta_{2s} = 1$ . Compared to standard carbon, the radial 2p valence wavefunction of design carbon is therefore depressed outside the core radius, and exalted within, to accommodate the extra electron, figure (5a). In fact Xiao and Zhang adjusted  $\eta_{2s}$ , optimising it with respect to the geometrical parameters of their target molecules, yielding in their case  $\eta_{2s} = 0.91$ . Our implementation closely follows ref. [32], and indeed our design carbon pseudo-potentials agree very closely with those of Xiao and Zhang, see figure (5b).

We extended the design atom approach to truncation on oxygen. In this case,  $\eta_{2p} = \sqrt{4/5} \sim 0.89$ . We varied  $\eta_{2s}$  in a series of truncations on the oxygen atom of the toy benzyl carbamate in figure (6a), similar in structure to graftable photosensitizers of reactive oxygen species of interest to us[22]. Here, we show results for  $\eta_{2s} = 1$ ; reducing it deteriorated the results. Figure (6b) compares the geometries of the full and the truncated forms, both fully optimised (LDA, standard DZP basis). The important part of the molecule is the phenyl ring, standing in for the chromophore. Our measure of quality is therefore to bring three phenyl carbons (atoms 4,1 and 3 in fig. 6a), of both the full and the truncated molecules, respectively to the origin, on to the  $Ox$  axis and into the  $Oxy$  plane, and to compute the distances between corresponding atoms, shown in fig. (6b) as a scatter plot of error *vs.* distance to the oxygen atom before truncation. It will be observed that the error of placement of atoms in the fragment relative to the full molecule, drops off fast as a function of the distance from the design oxygen, being under  $10^{-2}$  Å for those in the ring. Complete  $Z$ -matrices are provided in the supplementary information.

## 2.4 Linear response TDDFT

### Context

A new, order  $O(N^3)$  TDDFT code was described recently [14, 15, 21], exploiting the strictly finite range of the numerical atomic orbitals in SIESTA. The optical absorption of a molecule, for a light electric field at angular frequency  $\omega$ , polarised in the  $\alpha$  direction ( $\alpha = x, y, z$ ), is proportional to the complex part of the polarisability

$$P_\alpha(\omega) = \int d^3\mathbf{r} d^3\mathbf{r}' \mathbf{r}_\alpha \chi(\mathbf{r}, \mathbf{r}', \omega) \mathbf{r}'_\alpha, \quad (5)$$

where  $\chi(\mathbf{r}, \mathbf{r}', \omega)$  is the susceptibility, and we use the fact that molecules are much smaller than the wavelength. The susceptibility  $\chi$  is expressed in terms of that of the non-interacting electrons in the Kohn-Sham approach,  $\chi_0$ , and the Hartree and exchange-correlation kernel  $\Sigma$ :

$$\chi(\omega) = (1 - \chi_0(\omega) \Sigma)^{-1} \chi_0(\omega). \quad (6)$$

The non-interacting electron response function  $\chi_0$ , reads in terms of Kohn-Sham orbitals:

$$\begin{aligned} \chi_0(\mathbf{r}, \mathbf{r}', \omega) &= \sum_{E < 0, F > 0} \psi_E(\mathbf{r}) \psi_F(\mathbf{r}) \psi_F(\mathbf{r}') \psi_E(\mathbf{r}') \\ &\times \left( \frac{1}{\omega - (E - F) + j\epsilon} - \frac{1}{\omega + (E - F) + j\epsilon} \right), \end{aligned} \quad (7)$$

where the sum runs over transitions between filled and empty orbitals with energies  $E$  and  $F$ ,  $j^2 = -1$ , and  $\epsilon$  is a regularisation parameter. Since the orbitals  $\psi_E$  may be expressed as linear combinations of atomic orbitals (AO's), this form of  $\chi_0$  exhibits dependence on AO pair products.

References [14, 15] point out the high degree of linear dependence in the AO product space and the means to drastically reduce it by expressing AO products as linear combinations of dominant products found by diagonalisation of an appropriate metric. Paper [21] avoids explicit inversion in eqn. (6) and introduces an efficient parallel solution of the relevant equations:

$$\begin{cases} P(\omega) = \sum_{i=1}^3 \langle d_i, X_i(\omega) \rangle \\ (1 - \chi^0(\omega) \Sigma) X_i(\omega) = \chi^0(\omega) d_i, \quad i = 1, 2, 3 \end{cases} \quad (8)$$

where  $d_i$  is the dipole in the  $i$ -direction. Each linear system is solved by the Krylov GMRES method[26]. Solution of eqns. (8) at a set of frequencies  $\omega$  leads to a raw absorption spectrum.

Note that because  $\epsilon$  is a regularisation parameter, the raw spectrum for a particular value of  $\epsilon$  has no absolute physical meaning. Figure (7) shows how, given sufficient points in the raw spectrum, close resonances are distinguishable as the regularisation parameter is reduced. For convenience of representation, we plot  $\epsilon P_\epsilon(\omega)$  rather than  $P_\epsilon(\omega)$ , which diverges at resonances as  $\epsilon \rightarrow 0$ . Finding with any certainty even just the main resonances in a given frequency interval  $[\omega_{min}, \omega_{max}]$  would seem to require making  $\epsilon$  very small and using a very large number of points, of order  $(\omega_{max} - \omega_{min})/\epsilon$ . However, quite apart from the computational cost, it is ineffective to try to separate close resonances by brute force reduction of  $\epsilon$  and increasing the number of frequency points  $\omega$ . Close to resonances of the free electron response,  $\omega \sim E - F$  in eqn. (7),  $\chi_0$  diverges as  $1/\epsilon$  and ill-conditioning may prevent convergence of the GMRES method. We have observed slow convergence, or absence of convergence, or even negative polarisabilities at some

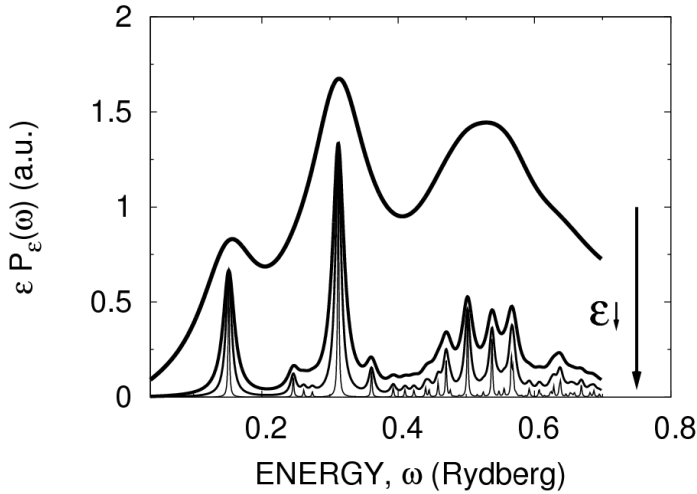


Figure 7: Absorption spectra of indigo computed with regularly spaced frequency points and decreasing regularisation parameter  $\epsilon=0.05, 0.01, 0.005$  and  $0.001$  Rydberg, from top to bottom.

frequency points when  $\epsilon$  is reduced below  $5 \times 10^{-4}$  Ry. There is no clear way to preconditioning the linear systems (8), so some other strategy is needed.

Furthermore, the method as it stands has other drawbacks: (i) The shape of the spectrum depends on the regularisation parameter  $\epsilon$ . When it is too big, a weak transition may go unnoticed in the wing of a strong one; but making it too small is wasteful, with most values of  $P(\omega)$  very small compared to a handful of large values at the resonances; (ii) Little can be done to identify the nature of the transitions observed in the spectrum, since not even oscillator strengths are extracted; (iii) The TDDFT computation is run after SIESTA, requiring geometrical, orbital, Hamiltonian and overlap data to be communicated in a disk file.

### Present improvements

An immediate step to improving separation of resonances is to deal separately with each polarisation in eqn. (8), since transitions often have different polarisations. Here we further improved the computation in several ways.

First, addressing point (iii), the 'FAST' TDDFT calculation can be invoked now from within SIESTA, the 'move' loop of the SIESTA main program. This is achieved by coupling FAST directly to SIESTA using the MPICPL (MPI Coupling) framework[3]. MPICPL is dedicated to the coupling of scientific codes, based on the well-known MPI standard. It is divided into several independent layers for coupling, data redistribution and steering. The codes to be coupled are launched and connections between them are set up by mpicpl, according to information derived from an xml file.

Second, to address points (i) and (ii), note that the expected form of the spectrum is a sum of Lorentzian resonances. By fitting the parameters of these Lorentzians to the numerical spectrum, we can in most cases identify the transitions without recourse to small  $\epsilon$  and very fine combs of  $\omega$  values. We relate the peak heights of the numerical spectrum to the oscillator strengths of the transitions by considering that in the linear response regime, electronic transitions respond to

the driving field like independent harmonic oscillators [24], so that the susceptibility

$$\chi(\omega) = \chi'(\omega) + j\chi''(\omega)$$

can be written in atomic units as

$$\chi(\omega) = \sum_I \frac{f_I}{\Omega_I^2 - \omega^2 - 2j\omega\Gamma_I},$$

where  $\Omega_I$ ,  $f_I$  and  $\Gamma_I$  are the frequency, oscillator strength and damping (homogeneous linewidth) of transition  $I$ . Here, we need the complex part of the susceptibility,  $\chi''(\omega)$ , which after a little algebra can be expressed as a sum of terms of the form

$$\frac{2\omega\Gamma_I f_I}{(\Omega_I - \omega)^2(\Omega_I + \omega)^2 + 4\omega^2\Gamma_I^2}.$$

Close to a resonance (elsewhere the susceptibility is negligible),  $\omega \sim \Omega_I$ , and  $\Omega_I + \omega \sim 2\omega \sim 2\Omega_I$ , so that

$$\chi''(\omega) \sim \sum_I \frac{f_I\Gamma_I/2\Omega_I}{(\Omega_I - \omega)^2 + \Gamma_I^2}.$$

Identifying the regularisation parameter  $\epsilon$  in the linear response TDDFT with the damping  $\Gamma_I$ , we see that the numerical spectrum should be representable as a sum of normalised (unit area) Lorentzian resonances,

$$\chi''_{\text{model}}(\omega) \sim \sum_{I=1}^{N_{\text{res}}} \frac{C_I\epsilon/\pi}{(\Omega_I - \omega)^2 + \epsilon^2} + B, \quad (9)$$

where the weights  $C_I$  are related to the oscillator strengths by

$$\frac{f_I}{2\Omega_I} = \frac{C_I}{\pi}.$$

In eqn. (9),  $B$  represents the more or less flat contribution of resonances outside the frequency range  $[\omega_{\min}, \omega_{\max}]$  where the raw spectrum was computed. We perform a non-linear least squares fit of the parameters  $C_I$ ,  $\Omega_I$  and  $B$  to minimise the residual:

$$\chi^2 = \frac{1}{N_{\text{freq}}} \sum_{j=1}^{N_{\text{freq}}} (\chi''_{\text{model}}(\omega_j) - I_j)^2, \quad (10)$$

using the Levenberg-Marquardt method from the GNU scientific library [1] and  $N_{\text{freq}}$  frequency points  $\omega_j$  in the numerical TDDFT spectrum, with intensities  $I_j$ .

Fitting a Lorentzian requires at least four data points. If  $N_L$  resonances are expected in the frequency range  $[\omega_{\min}, \omega_{\max}]$ , the raw spectrum should comprise at least  $N_{\text{freq}} = N_1 = 4N_L$  points. A reasonable trial  $\epsilon$  would be  $\epsilon = \epsilon_1 = (\omega_{\max} - \omega_{\min})/N_1$ . The number of certain resonances and their positions are determined by an inspection algorithm detecting local maxima of the spectrum from adjacent regions of increasing or decreasing values. Clearly, the smaller the value of  $\epsilon$ , the sharper the resonances will become, and the greater will be the number of distinguishable resonances. But because of the *caveat* noted above and of the computational cost,  $\epsilon$  should not be made too small.

The question now is how to best choose the  $\omega_j$ . In practice, data in the wings of the resonances contribute less to the accuracy of the Lorentzian fit than do points close to the peaks. Since the resonances are at first unknown, one must start with a uniform distribution of  $\omega_j$  but it



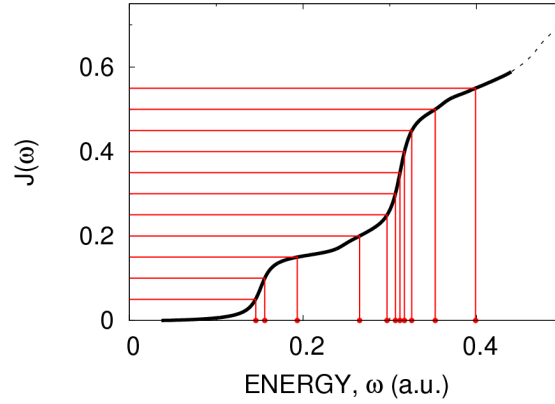


Figure 8: Behaviour of the integral function  $J(\omega)$  used to concentrate TDDFT computation points  $\omega_j$  around the resonances of the current best estimate of the spectrum (in this case the top spectrum in figure 7).

is possible to continue with an iterative, adaptive procedure, to cluster the points around the current best approximations to the resonance frequencies.

With this purpose, define a normalized integral function as

$$J(\omega) = \int_{\omega_{\min}}^{\omega} P(\omega) d\omega \Big/ \int_{\omega_{\min}}^{\omega_{\max}} P(\omega) d\omega . \quad (11)$$

As  $P$  is a positive function,  $J$  increases monotonically (from 0 to 1) as  $\omega$  sweeps the interval  $[\omega_{\min}, \omega_{\max}]$ . In practice,  $J(\omega)$  increases step-wise at each resonance, the smaller the value of  $\epsilon$ , the steeper the steps and the flatter the plateaux between the steps, see fig. (8). Therefore, we can easily construct a local inverse function where  $P$  is non zero. The trick is now to use the inverse function to map a set of regularly spaced values of  $J$  into a set  $\omega$ 's clustered around the resonances. Since at any time we know only a finite number of  $(\omega_i, J(\omega_i))$  pairs, the local inverse function is defined *via* linear interpolation:

$$J_{\text{approx}}(\omega) = J(\omega_i) \frac{J(\omega_{i+1}) - J(\omega_i)}{\omega_{i+1} - \omega_i} (\omega - \omega_i) \quad \omega \in [\omega_i, \omega_{i+1}]. \quad (12)$$

Figure (8) illustrates this procedure for the topmost spectrum ( $\epsilon = 0.05$  a.u.) in figure (7).

The complete algorithm is provided in the supplementary information, with results for uniformly spaced data. Briefly, we start with a uniform distribution of points and iterate the clustering around the current best estimates of the resonances. At each stage of the procedure, the number of certain resonances to be used in the fit is determined by inspection of the numerical spectrum, and the inverse integral function is used to improve the distribution of the points around these resonances before refitting the Lorentzians. After iterating the improvement of the distribution of points, the algorithm may decrease  $\epsilon$  or increase the number of points, or do both.

### Application to indigo

Before going into more detail about the choice of adaptive strategies in the algorithm, figure (9) validates the present approach. It shows results for a set of substituted benzenes. The

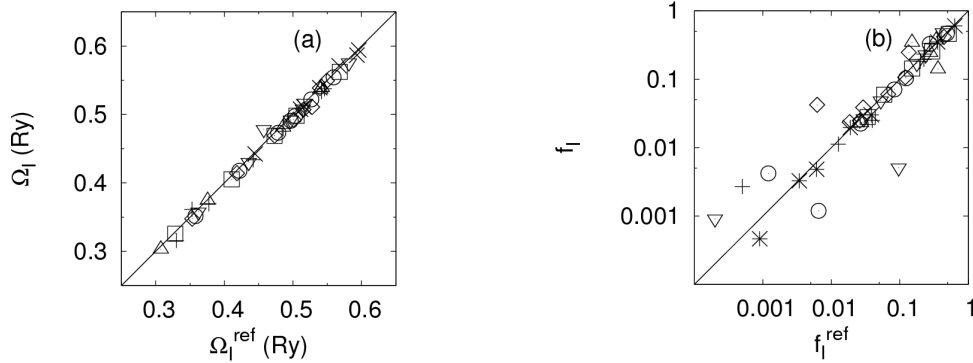


Figure 9: Comparison of transitions obtained with the present adaptive algorithm (LDA, numerical DZP basis, vertical axis) to those obtained by solution of Casida’s eigenproblem equations (LSD, 6-31G\*, horizontal axis), for a series of substituted benzenes. (a) Transition energies; (b) oscillator strengths. Symbols :  $\square$  aniline;  $\circ$  anisole;  $\triangle$  dimethylaniline;  $\nabla$  phenol;  $\diamond$  phentole;  $+$  thiophenol;  $\times$  toluene .

figure compares transition energies and oscillator strengths obtained here (LDA, standard DZP valence basis and pseudo-potentials in SIESTA) to those obtained with a similar level of theory (LSD, 6-31G\* all electron basis) by solving Casida’s eigenproblem casting of linear response theory[10, 20, 17]. Calculations were performed on the same geometries, optimised in SIESTA. Despite differences in the basis sets, the agreement is good, including even most of the weaker transitions.

Table 1 illustrates four ways to use the adaptive fitting to improve the accuracy on the transitions obtained for the visible spectrum of indigo in the range 0.02 to 0.4 Ry, computed with the same DFT conditions as in section 2.2. The final value of the regularization parameter is in each case  $\epsilon = 10^{-3}$  Ry. Table 1 shows two strategies. Cases 1–4 illustrate constant  $\epsilon$  ( $10^{-3}$  Ry) and variable placing or numbers of data points. In case 5, both  $\epsilon$  and the number of data points are varied, the latter being determined by  $\epsilon$ . The idea, here is to use fewer points placed depending on the regularized parameter. We summarize below the parameters of the different strategies :

*Test 1* Here, the number of points is constant and we iteratively improve the point placement. Considering that resonances will not be separable if closer than  $\epsilon$ , up to

$$N_{\text{trans}} \sim (\omega_{\text{max}} - \omega_{\text{min}})/2\epsilon \quad (13)$$

resonances could in principle be distinguished, given 4 points for each. The minimum number of points required is thus:

$$N_{\text{freq}} = 1 + \frac{3}{2\epsilon}(\omega_{\text{max}} - \omega_{\text{min}}). \quad (14)$$

*Test 2* and *test 3* are the same as test 1, but use fewer points, respectively 285 and 101.

*Test 4* starts with the same small number of points as *test3*, and at each iteration  $N_{\text{freq}}$  is increased by 25%.

	Test 1	test 2	test 3	test 4	test 5
$\epsilon^{\text{initial}}$ (Ry)	$1 \times 10^{-3}$	$1 \times 10^{-3}$	$1 \times 10^{-3}$	$1 \times 10^{-3}$	$2 \times 10^{-2}$
$\epsilon^{\text{final}}$ (Ry)	$1 \times 10^{-3}$	$1 \times 10^{-3}$	$1 \times 10^{-3}$	$1 \times 10^{-3}$	$1 \times 10^{-3}$
$N_{\text{freq}}^{\text{initial}}$	571	285	101	101	50
$N_{\text{freq}}^{\text{final}}$	571	285	101	198	255
$N_{\text{iter}}$	2	2	5	4	5
$N_{\text{eval}}$	1142	570	505	583	663
$N_{\text{trans}}$	7	7	4	6	7
$\chi/  I  _2$	$3.0 \times 10^{-4}$	$3.4 \times 10^{-4}$	$1.7 \times 10^{-3}$	$5.9 \times 10^{-3}$	$4.2 \times 10^{-4}$
$\delta f_{\text{max}}$	$2.2 \times 10^{-4}$	$2.1 \times 10^{-5}$	$1.0 \times 10^{-4}$	$8.9 \times 10^{-4}$	$6.2 \times 10^{-4}$

Table 1: Statistics of different iterative strategies to improve the fitting of Lorentzians to the numerical TDDFT spectrum of indigo.  $N_{\text{freq}}^{\text{initial}}$ ,  $N_{\text{freq}}^{\text{final}}$ : initial and final numbers of data points;  $N_{\text{iter}}$ : number of iterations to reach an error of  $5.0 \times 10^{-2}$  Ry;  $N_{\text{eval}}$ : total number of evaluations of  $P(\omega)$  at convergence;  $N_{\text{trans}}$ : number of transitions found;  $\chi^2$ : the residual defined by eqn. (10).  $\delta f_{\text{max}}$  is the maximum variation of the oscillator strengths between the last two iterations at convergence.

*Test 5* starts with  $\epsilon = 2 \times 10^{-2}$  Ry and  $N_{\text{freq}} = 50$  and  $\epsilon$  is reduced in equal steps to  $10^{-3}$  Ry in two iterations. At each iteration the number of points increases by 25 % in order to have enough points for the fit algorithm.

Table 1 shows the consequences of these strategies. *Test 1* represents a brute force approach. But most real molecules will have far fewer transitions than implied by eqn (13). Accordingly, *tests 2-3* show that the number of points can be reduced without loss of information, but that eventually (*test 3*) some weak transitions are missed. These are recovered in *test 4*, where data points are added, but only as necessary. The number of evaluations of  $P(\omega)$  is half that required by brute force, for a comparable result. *Test 5* achieves an even better result, at the expense of slightly more function evaluations, by decreasing  $\epsilon$ .

Figure 10 shows the spectrum and the fits obtained in *tests 4* and *5*. Resonances found in the tests agree very well, to within about  $10^{-5}$  Ry ( $4 \text{ cm}^{-1}$ ) for the resonance frequency and about 0.1 % for the oscillator strengths. These results illustrate a further benefit of the fitting procedure, that, using a moderate  $\epsilon$  ( $10^{-3}$  Ry), it achieves an accuracy that could only be achieved by brute force with much smaller  $\epsilon$ , for which the TDDFT algorithm would be numerically unstable. The energy and oscillator strength of the first excited state of indigo are 0.1515 Ry (or a wavelength of 602 nm in vacuum) and 0.2, values which could certainly be improved (the experimental transition is at 0.136 Ry or 546 nm[27]), should hybrid functionals become available in SIESTA.

### 3 Concluding remarks

We have described several extensions of the widely used SIESTA program, aimed at making it more directly applicable to molecular systems. Some closing words may be appropriate on the methods chosen.

Self polarisation in the periodic model of an isolated water molecule was small. However, larger effects can be expected for systems which are both polar and contain  $\pi$  electrons, such as

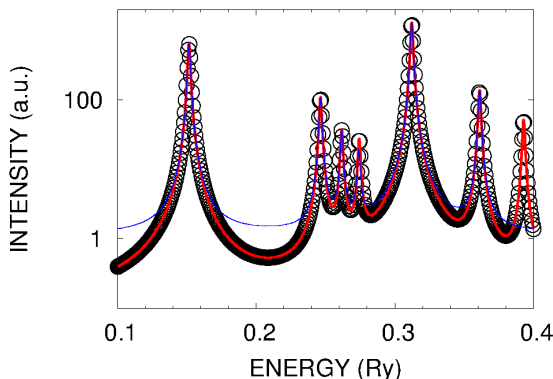


Figure 10: The UV-visible part of the absorption spectrum of indigo; semi-log scale to highlight strong and weak resonances. Data points : numerical spectrum; thin line : the Lorentzian fit of test 4 misses the highest energy resonance, which is recovered in test 5 (thick line).

many common laser dyes, in which a degree of intramolecular charge transfer is present, even in the ground state. Large dipole moments are common in laser dyes, which moreover may contain 20–40 heavy atoms. Simulation boxes big enough to effectively separate such systems from their images could become uncomfortably large. The present multi-grid solver for the Poisson equation with Dirichlet boundary conditions meets this need, in a framework that should make further improvements possible, such as use of finite elements to represent the usually inhomogeneous electronic density.

Electrostatic potential fitting is an old problem, with a vast literature. The algorithm introduced here in SIESTA is very simple. While it so far has worked satisfactorily for molecules of interest to us, general users should be aware that it may produce unpredictable results on systems with 'buried' atoms. The algorithm here has also been adapted to fit the electrostatic potential computed in SIESTA in periodic systems. See however Campaña *et al.*[9] for a lucid discussion of the problems associated with charge fitting in such systems.

The design atom approach to truncation of molecules does not appear to have been taken up in the literature, possibly because Xiao and Zhang exhibited significant perturbation of the truncated moieties of *small* molecules[32]. Indeed, we too found for example that dihedrals close to the design atom may be in error by 10–20°. Yet, as shown here, the perturbation in fact decays rapidly with distance from the design atom, making the method attractive for truncation of large systems.

It should also be mentioned that the lone pair of the design atom may give rise to spurious  $n - \pi^*$  transitions towards a conjugated region of the truncated molecule. They appear as weak transitions in the low energy wing of the spectrum, with intensities falling off exponentially with the distance to the design atom. This easily identified effect is tolerable in large molecules, in view of the gain in computational cost brought by truncation. A typical case would be truncation in quantum mechanical/classical mechanical simulations, where a number of other approximations might be more serious than the presence of these weak but identified transitions

It may be useful to put the linear-response TDDFT method in refs. [14, 15, 21] and the present improvements in perspective with commoner approaches, such as for example Casida's widely implemented equations[10, 20]. The point is that whereas solution of Casida's equations yields at significant cost a list of transitions and their properties, the linear response TDDFT method

produces a piece of the raw spectrum, at low cost, but with little physical insight, such as orbital symmetries and energies, transition polarisations and oscillator strengths.

The present extensions, by efficiently extracting transition energies, oscillator strengths and a degree of polarisation information, should be useful to identify transitions by comparison with a one-off solution of Casida's equations for the same system. The strength of the present method would then be to allow cheap, repetitive calculations to study how the transition reacts to multiple perturbations of the geometry, or a varying external field, because  $P(\omega)$  then needs to be computed only in narrow frequency intervals bracketing the interesting resonances. Indeed, useful experimental data are in the vast majority of cases restricted to the first one or two strongest excited states only. For example, the first transition of indigo on a recent 12-core computer could be computed in less 30s of which over 90% of time was spent building the Hartree and exchange-correlation contributions (half each) to the interaction kernel. The cost of the iterative procedure was negligible. Computing spectra on the fly during molecular dynamics, *e.g.* solvation shifts in liquids, is thus a realistic prospect of the present methods.

**Acknowledgements.** It is pleasure to thank members of the SIESTA development team, particularly Alberto García, ICMAB, Barcelona, for their encouragement and advice. Part of the calculations were performed at the high performance computing facility MCIA: Mésocentre de calcul intensif en Aquitaine and on the PlaFRIM experimental testbed, developed under the Inria PlaFRIM development action with support from LABRI and IMB and other entities: Conseil Régional d'Aquitaine, FeDER, Université de Bordeaux and CNRS (see <https://plafrim.bordeaux.inria.fr/>).

## References

- [1] GSL - GNU Scientific Library. [Http://www.gnu.org/software/gsl](http://www.gnu.org/software/gsl)
- [2] hypre: High performance preconditioners. <http://www.llnl.gov/CASC/hypre>
- [3] MPICPL: MPI coupling. <https://gforge.inria.fr/projects/mpicpl/>
- [4] hypre User's manual, version 2.0.0 (2006). Center for Applied Scientific Computing, Lawrence Livermore National Laboratory, Livermore, CA 94550
- [5] Anderson, E., Bai, Z., Bischof, C., Blackford, S., Demmel, J., Dongarra, J., Du Croz, J., Greenbaum, A., Hammarling, S., McKenney, A., Sorensen, D.: LAPACK Users' Guide, third edn. Society for Industrial and Applied Mathematics, Philadelphia, PA (1999)
- [6] Artacho, E., Anglada, E., Dieguez, O., Gale, J.D., García, A., Junquera, J., Martin, R.M., Ordejón, P., Pruneda, J.M., Sánchez-Portal, D., Soler, J.M.: The siesta method; developments and applicability. *J. Phys.: Condens. Matter* **20**, 064,208–1–6 (2008)
- [7] Bayly, C.I., Cieplak, P., Cornell, W.D., Kollman, P.A.: A well-behaved electrostatic potential based method using charge restraints for deriving atomic charges: the resp method. *J. Phys. Chem.* **97**, 10,269–10,280 (1993)
- [8] Briggs, W.L., Henson, V.E., McCormick, S.F.: A Multigrid Tutorial. Siam, Philadelphia, PA (2000)
- [9] Campaña, C., Mussard, B., Woo, T.K.: Electrostatic potential derived atomic charges for periodic systems using a modified error functional. *J. Chem. Theory Comput.* **5**, 2866–2878 (2009)

- [10] Casida, M.E.: Time dependent density functional response theory for molecules. In: D.P. Dong (ed.) Recent advances in density functional methods, part I, Recent advances in computational chemistry, pp. 155–192. World Scientific, Singapore (1995)
- [11] Connolly, M.L.: Analytical molecular surface calculation. *Journal of Applied Crystallography* **16**(5), 548–558 (1983)
- [12] Falgout, R.D., Jones, J.E.: Multigrid on massively parallel architectures. In: E. Dick, K. Riemsdagh, J. Vierendeels (eds.) Multigrid Methods VI, *Lecture Notes in Computational Science and Engineering*, vol. 14, pp. 101–107. Springer, Berlin (2000). Proc. of the Sixth European Multigrid Conference held in Gent, Belgium, September 27–30, 1999. Also available as LLNL technical report UCRL-JC-133948
- [13] Falgout, R.D., Jones, J.E., Yang, U.M.: The design and implementation of *hypre*, a library of parallel high performance preconditioners. In: A.M. Bruaset, A. Tveito (eds.) Numerical Solution of Partial Differential Equations on Parallel Computers, pp. 267–294. Springer-Verlag (2006). Also available as LLNL technical report UCRL-JRNL-205459
- [14] Foerster, D.: Elimination, in electronic structure calculations, of redundant orbital products. *J. Chem. Phys.* **128**, 034,108–1–9 (2008)
- [15] Foerster, D., Koval, P.: On the Kohn-Sham density response in a localized basis set. *J. Chem. Phys.* **131**, 044,103–1–9 (2009)
- [16] Francl, M.M., Carey, C., Chirlian, L.E.: Charges fit to electrostatic potentials. ii. Can atomic charges be unambiguously fit to electrostatic potentials. *J. Comp. Chem.* **17**, 367–383 (1996)
- [17] Frisch, M.J., Trucks, G.W., Schlegel, H.B., Scuseria, G.E., Robb, M.A., Cheeseman, J.R., Scalmani, G., Barone, V., Mennucci, B., Petersson, G.A., Nakatsuji, H., Caricato, M., Li, X., Hratchian, H.P., Izmaylov, A.F., Bloino, J., Zheng, G., Sonnenberg, J.L., Hada, M., Ehara, M., Toyota, K., Fukuda, R., Hasegawa, J., Ishida, M., Nakajima, T., Honda, Y., Kitao, O., Nakai, H., Vreven, T., Montgomery Jr., J.A., Peralta, J.E., Ogliaro, F., Bearpark, M., Heyd, J.J., Brothers, E., Kudin, K.N., Staroverov, V.N., Kobayashi, R., Normand, J., Raghavachari, K., Rendell, A., Burant, J.C., Iyengar, S.S., Tomasi, J., Cossi, M., Rega, N., Millam, J.M., Klene, M., Knox, J.E., Cross, J.B., Bakken, V., Adamo, C., Jaramillo, J., Gomperts, R., Stratmann, R.E., Yazyev, O., Austin, A.J., Cammi, R., Pomelli, C., Ochterski, J.W., Martin, R.L., Morokuma, K., Zakrzewski, V.G., Voth, G.A., Salvador, P., Dannenberg, J.J., Dapprich, S., Daniels, A.D., Farkas, Á., Foresman, J.B., Ortiz, J.V., Cioslowski, J., Fox, D.J.: Gaussian 09 Revision A.1. Gaussian Inc. Wallingford CT 2009
- [18] Greengard, L., Rokhlin, V.: A fast algorithm for particle simulations. *Journal of Computational Physics* **73**(2), 325 – 348 (1987)
- [19] Jackson, J.D.: Classical Electrodynamics, third edn. Wiley (1998)
- [20] Jamorski, C., Casida, M.E., Salahub, D.R.: Dynamic polarizabilities and excitation spectra from a molecular implementation of time-dependent density-functional response theory: N<sub>2</sub> as a case study. *J. Chem. Phys.* **104**, 5134–5147 (1996)
- [21] Koval, P., Foerster, D., Coulaud, O.: A parallel iterative method for computing molecular absorption spectra. *J. Chem. Theory Comput.* **6**, 2654–2668 (2010)

- 
- [22] Lacombe, S., Soumillion, J.P., El Kadib, A., Pigot, T., Blanc, S., Brown, R., Oliveros, E., Cantau, C., Saint-Cricq, P.: Solvent-free production of singlet oxygen at the gas-solid interface: Visible light activated organic-inorganic hybrid microreactors including new cyanoaromatic photosensitizers. *Langmuir* **25**(18), 11,168–11,179 (2009)
- [23] Lawson, C.L., Hanson, R.J., Kincaid, D.R., Krogh, F.T.: Basic linear algebra subprograms for fortran usage. *ACM Trans. Math. Softw.* **5**(3), 308–323 (1979)
- [24] Mukamel, S.: Principles of nonlinear optical spectroscopy. O.U.P., New York (1995)
- [25] Perdew, J.P., Zunger, A.: Self-interaction correction to density-functional approximations for many-electron systems. *Phys. Rev. B* **23**, 5048–5079 (1981)
- [26] Saad, Y.: Iterative Methods for Sparse Linear Systems. Siam, Philadelphia (2003)
- [27] Sadler, P.W.: Absorption spectra of indigoid dyes. *J.Org. Chem.* **21**, 316–318 (1956)
- [28] Sanz-Navarro, C.F., Grima, R., García, A., Bea, E.A., Soba, A., Cela, J.M., Ordejón, P.: An efficient implementation of a QM-MM method in SIESTA. *Theor. Chem. Acc.* **128**, 825–833 (2011)
- [29] Sigfridsson, E., Ryde, U.: Comparison of methods for deriving atomic charges from the electrostatic potential and moments. *J. Comp. Chem.* **19**, 377–395 (1998)
- [30] Soler, J.M., Artacho, E., Gale, J.D., García, A., Junquera, J., Ordejón, P., Sánchez-Portal, D.: The Siesta method for ab initio order-n materials simulation. *J. Phys.: Condens. Matter* **14**, 2745–2779 (2002)
- [31] Terrabuio, L.A., Haiduke, R.L.A.: Electrostatic potentials and polarization effects in proton-molecule interactions by means of multipoles from the quantum theory of atoms in molecules. *International Journal of Quantum Chemistry* **112**(19)
- [32] Xiao, C., Zhang, Y.: Design-atom approach for the quantum mechanical/molecular mechanical covalent boundary: A design-carbon atom with five valence electrons. *J. Chem. Phys.* **127**, 124,102–1–9 (2007)

## Supplementary Information

### 1 Linear scaling of the MG solver of the Poisson equation

Figure 11 shows the linear dependence of the sequential execution time of the MG solver on the size of the problem.

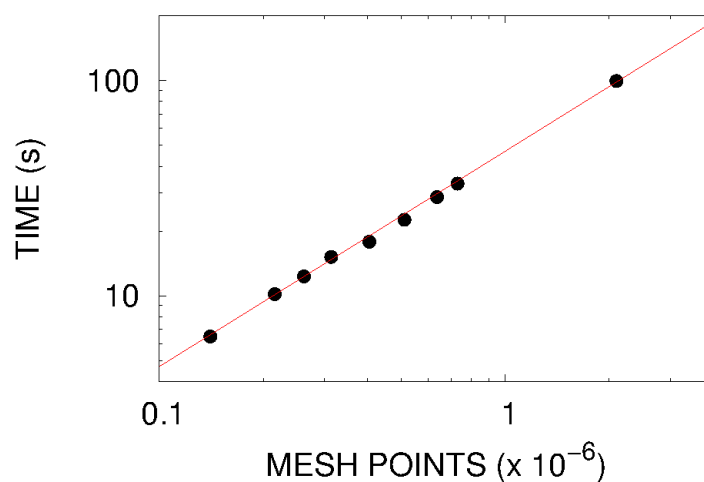


Figure 11: Log-log plot of the CPU time (sequential, Nehalem Intel Xeon X5550, 2.66 GHz) of the multi-grid solution of the Poisson equation *vs.* system size. Line shows linear scaling.

### 2 Use of the O design atom

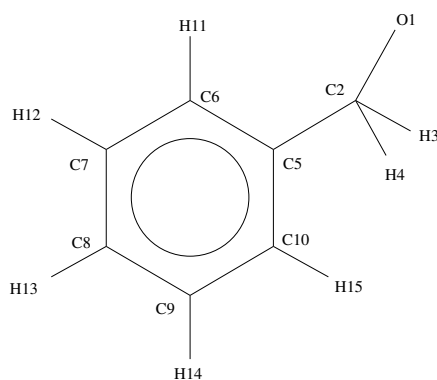


Figure 12: Atomic numbering used to compare the  $Z$ -matrices.



The  $Z$ -matrices of the optimised geometries (DZP, LDA, standard Troullier-Martins pseudopotentials) of the full benzylcarbamide and the truncated form are provided below. Atom numbers differ from the main text; refer figure 12 above.

### $Z$ -matrix full molecule

```
c
c 1 cc2
c 2 cc3      1 ccc3
c 3 cc4      2 ccc4      1 dih4
c 4 cc5      3 ccc5      2 dih5
c 5 cc6      4 ccc6      3 dih6
c 2 cc7      3 ccc7      4 dih7
o 7 oc8      2 occ8      3 dih8
h 7 hc9      2 hcc9      3 dih9
h 7 hc10     2 hcc10     3 dih10
h 3 hc11     2 hcc11     7 dih11
h 4 hc12     3 hcc12     2 dih12
h 5 hc13     4 hcc13     3 dih13
h 6 hc14     5 hcc14     4 dih14
h 1 hc15     2 hcc15     7 dih15

cc2      1.396646
cc3      1.391612
ccc3     119.687
cc4      1.395160
ccc4     119.692
dih4     0.093
cc5      1.392020
ccc5     120.426
dih5     -0.104
cc6      1.393252
ccc6     119.826
dih6     0.108
cc7      1.483357
ccc7     123.223
dih7     179.682
oc8      1.411371
occ8     112.767
dih8     -4.392
hc9      1.118685
hcc9     112.372
dih9     117.630
hc10     1.118928
hcc10    109.421
dih10    -124.994
```

hc11	1.106000
hcc11	117.974
dih11	-0.028
hc12	1.103650
hcc12	120.114
dih12	-179.891
hc13	1.103440
hcc13	120.430
dih13	-179.685
hc14	1.103566
hcc14	120.486
dih14	-179.925
hc15	1.105580
hcc15	119.052
dih15	0.187

#### Z--matrix Truncated molecule

c			
c	1 cc2		
c	2 cc3	1 ccc3	
c	3 cc4	2 ccc4	1 dih4
c	4 cc5	3 ccc5	2 dih5
c	5 cc6	4 ccc6	3 dih6
c	2 cc7	3 ccc7	4 dih7
o	7 oc8	2 occ8	3 dih8
h	7 hc9	2 hcc9	3 dih9
h	7 hc10	2 hcc10	3 dih10
h	3 hc11	2 hcc11	7 dih11
h	4 hc12	3 hcc12	2 dih12
h	5 hc13	4 hcc13	3 dih13
h	6 hc14	5 hcc14	4 dih14
h	1 hc15	2 hcc15	7 dih15
cc2	1.396569		
cc3	1.392214		
ccc3	119.781		
cc4	1.392371		
ccc4	120.107		
dih4	0.046		
cc5	1.391827		
ccc5	120.063		
dih5	-0.082		
cc6	1.393444		
ccc6	119.910		

dih6	0.038
cc7	1.489138
ccc7	118.945
dih7	-179.458
oc8	1.429060
occ8	110.379
dih8	-4.063
hc9	1.117354
hcc9	110.988
dih9	114.752
hc10	1.117136
hcc10	111.543
dih10	-123.507
hc11	1.107117
hcc11	116.267
dih11	0.794
hc12	1.103764
hcc12	120.342
dih12	-179.991
hc13	1.103441
hcc13	120.126
dih13	-179.768
hc14	1.104104
hcc14	119.974
dih14	-179.783
hc15	1.105587
hcc15	120.026
dih15	-0.564

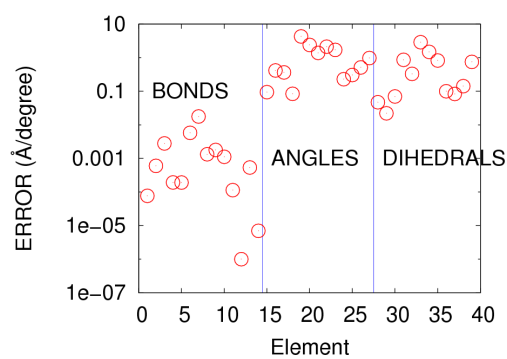


Figure 13: Errors of internal coordinates of the truncated *vs.* the full molecule (numbering, see *Z*-matrices and figure 12).

Figure 13 provides an overview of the errors in the different types of internal coordinates, with reference to the *Z*-matrices and the atomic numbering in figure 12 (not the same as in the main text).

### 3 Adaptive algorithm for fitting Lorentzians to the raw TDDFT spectrum

---

**Algorithm 1:** Adaptive algorithm
 

---

**Initialization** ( $p = 1$ ):

**begin**

Start with a small number  $N_1$  of uniformly distributed frequency points

$$\omega_j^1 = \omega_{\min} + (\omega_{\max} - \omega_{\min}) \times \frac{j-1}{N_p}$$

and a not too small value of  $\epsilon = \epsilon_1$ .

**for**  $it = 1, iterMax$  **do**

  Compute  $P$  on the current  $\omega_j$ .

**Build the new distribution:**

**begin**

    Define a set of uniformly spaced  $U_i = i/N_p, i = 1, \dots, N_p$  in  $[0,1]$ .

    Find  $\omega_i$  such that  $J(\omega_i) \leq U_i < J(\omega_{i+1})$

    The new improved frequency is  $\omega_i = J_{\text{approx}}^{-1}(U_i)$

**step Fit** Perform the least squares fit and determine the transitions  $\Omega_k$  and associated oscillator strengths  $f_k$ .

  Check the convergence:

$$\max \left( \max_{k < N_L} \|\Omega_k^{it} - \Omega_k^{it-1}\|, \max_{k < N_L} \|f_k^{it} - f_k^{it-1}\| \right) < \mu$$

  Reduce the regularization parameter if necessary.

---

The different steps of the adaptive algorithm are illustrated in Algorithm 1. We start the algorithm with a uniform distribution of points. In step Fit of Algorithm 1, first we determine the number of Lorentzian involved in the spectra, using a peak detection algorithm, inspecting for adjacent regions of increasing and decreasing values. The adaptive algorithm converges when the maximum difference between two iterations of the  $N_{\text{trans}}$  first (*i.e.* strongest) transition frequencies and the oscillator strengths are less than a given threshold  $\mu$ .

Tables 2 and 3 below provide additional data to complement the main text, on the amount of information recovered under different conditions in the spectrum of indigo in the range  $[0.02, 0.4]$  Ry. They show respectively, the influence of the regularisation parameter  $\epsilon$  at constant number of data points  $N_{\text{freq}} = 257$  and at minimal  $N_{\text{freq}} = 1 + \frac{3}{2\epsilon}(\omega_{\max} - \omega_{\min})$ . In both cases, the data points are distributed *uniformly*. The residual  $\chi^2$  is defined by

$$\chi^2 = |(I(\omega) - \chi''_{\text{Lorentzian}}(\omega))|_2 / |I(\omega)|_2,$$

where  $|\cdot|_2$  is the discrete  $l^2$  norm,  $\chi''_{\text{Lorentzian}}$  is the Lorentian approximation to the experimental data  $I(\omega)$ . All other calculation conditions are the same as in the main text.

$\epsilon$ (Ry)	Transitions recovered, $N_{\text{trans}}$	First transition		Second transition		$\chi^2$
		$\Omega_1$ (Ry)	$f_1$	$\Omega_2$ (Ry)	$f_2$	
0.5	0	-	-	-	-	0.45
0.1	1	0.322242	0.129389	-	-	0.48
0.075	1	0.318569	0.104083	-	-	0.48
0.05	2	0.318730	0.103203	0.163087	0.180037	0.62
0.025	2	0.313096	0.857635	0.153033	0.160789	0.15
0.01	5	0.312138	0.814819	0.151514	0.194918	$5.9 \times 10^{-2}$
0.0075	6	0.312170	0.812227	0.151501	0.196285	$5.5 \times 10^{-2}$
0.005	7	0.312170	0.810278	0.151497	0.196530	$4.2 \times 10^{-2}$
0.0025	7	0.312168	0.809110	0.151496	0.196621	$4.1 \times 10^{-2}$
0.001	10	0.312168	0.809302	0.151496	0.196691	$2.4 \times 10^{-3}$
0.00075	12	0.312168	0.809151	0.151496	0.196687	$1.9, 10^{-3}$
0.0005	10	0.312168	0.809377	0.151496	0.196662	$3.4 \times 10^{-3}$
0.00025	7	0.312169	0.807611	0.151497	0.196209	$3.8 \times 10^{-3}$
0.0001	13	0.310937	*	*	*	$\infty$

Table 2: Influence of  $\epsilon$  (at  $N_{\text{freq}} = 257$ ) on the frequency and oscillator strength recovered for the two strongest transitions of indigo in the interval  $[0.02, 0.4]$  Ry. - means nothing found, \* means wrong resultss (negative polarisability).

$\epsilon$ (Ry)	$N_{\text{freq}}$	Transitions recovered, $N_{\text{trans}}$	First transition		Second transition		$\chi^2$
			$\Omega_1$ (Ry)	$f_1$	$\Omega_2$ (Ry)	$f_2$	
0.1	6	0	-	-	-	-	0.48
0.075	8	0	-	-	-	-	0.48
0.05	12	0	-	-	-	-	0.62
0.025	23	2	0.312846	0.876805	0.153001	0.173854	0.14
0.01	58	4	0.312145	0.813828	0.151517	0.193658	$5.9 10^{-2}$
0.0075	77	4	0.312159	0.809740	0.151502	0.193412	$5.5 10^{-2}$
0.005	115	6	0.312170	0.808326	0.151497	0.195282	$4.2 10^{-2}$
0.0025	229	7	0.312168	0.809217	0.151496	0.196632	$4.0 10^{-2}$
0.001	571	11	0.310168	0.804095	0.149496	0.194092	$2.5 10^{-3}$
0.00075	761	13	0.309168	0.801070	0.148496	0.192807	$2.3 10^{-3}$
0.0005	1141	16	0.308168	0.798482	0.148830	0.193213	$1.7 10^{-3}$
0.00025	2281	23	0.307502	0.794531	0.149496	0.193877	$3.4 10^{-3}$
0.0001	5701	22	0.304964	0.726735	0.148896	0.191774	$\infty$

Table 3: Influence of  $\epsilon$ , automatic choice for the number of frequencies (- means nothing found.)



**RESEARCH CENTRE  
BORDEAUX – SUD-OUEST**

200 avenue de la Vieille Tour  
33405 Talence Cedex

Publisher  
Inria  
Domaine de Voluceau - Rocquencourt  
BP 105 - 78153 Le Chesnay Cedex  
[inria.fr](http://inria.fr)

ISSN 0249-6399